2D MATERIALS

Nematicity and competing orders in superconducting magic-angle graphene

Yuan Cao[1]*, Daniel Rodan-Legrain[1], Jeong Min Park[1], Noah F. Q. Yuan[1], Kenji Watanabe[2], Takashi Taniguchi[3], Rafael M. Fernandes[4], Liang Fu[1], Pablo Jarillo-Herrero[1]*

Strongly interacting electrons in solid-state systems often display multiple broken symmetries in the ground state. The interplay between different order parameters can give rise to a rich phase diagram. We report on the identification of intertwined phases with broken rotational symmetry in magic-angle twisted bilayer graphene (TBG). Using transverse resistance measurements, we find a strongly anisotropic phase located in a "wedge" above the underdoped region of the superconducting dome. Upon its crossing with the superconducting dome, a reduction of the critical temperature is observed. Furthermore, the superconducting state exhibits an anisotropic response to a direction-dependent in-plane magnetic field, revealing nematic ordering across the entire superconducting dome. These results indicate that nematic fluctuations might play an important role in the low-temperature phases of magic-angle TBG.

Spontaneous symmetry breaking is a ubiquitous process that occurs at all length scales in nature (*1*). In a solid-state system, besides time-reversal and gauge symmetries, there are certain discrete symmetries imposed by the underlying crystal lattice. However, these symmetries can be spontaneously broken when many-body electron-electron interactions in the system are appreciable. Understanding these broken-symmetry states is fundamental to elucidating the various phases in these many-body systems (*2*, *3*). One example is the electronic nematic phase, in which the discrete rotational symmetry of the lattice is spontaneously broken owing to electron correlations, although lattice translational and time-reversal symmetries are preserved (*4*, *5*). The resulting anisotropy of the system is in turn manifested in the properties involving spin, charge, and lattice degrees of freedom, which can be measured by scattering, transport, and scanning probe experiments (*6*–*11*).

When a correlated system has multiple broken-symmetry phases, their relationship often goes beyond mere competition, giving rise to a complex phase diagram of intertwined phases (*3*, *12*–*17*). An example of intertwined order is a nematic superconducting state, which simultaneously breaks lattice rotational and gauge symmetries. Nematic superconducting states have been reported in certain iron pnictides and in doped Bi_2Se_3, as revealed by thermal, magnetic, and transport measurements (*18*–*24*), although their microscopic origin is still unclear.

The recent discovery of correlated insulator and superconducting behaviors (*25*, *26*) in two-dimensional (2D) graphene superlattices brings the possibility of studying correlated superconducting materials with unmatched tunability and richness. Twisted 2D materials exhibit long-range moiré patterns in real space that can be tuned by the twist angle (Fig. 1A). In twisted bilayer graphene (TBG) near the first magic-angle $\theta \approx 1.1°$, the interlayer hybridization results in nearly flat bands at low energies, in which the electrons are localized in real space (Fig. 1A) (*27*–*29*). Near half-filling of the nearly flat bands, emergent correlated insulator behavior, and superconductivity have been demonstrated (*25*, *26*, *30*). In this work, we study the interplay between the superconducting phase and other many-body phases in magic-angle TBG. Compared to conventional materials, a major advantage of magic-angle TBG is that the band filling can be continuously tuned by electrostatic gating instead of chemical doping, so that different phases can be accessed in a single device.

Characterization of magic-angle graphene

Using the previously developed "tear and stack" dry-transfer technique (*31*, *32*), we fabricate high-quality encapsulated TBG devices with twist angles around the first magic angle $\theta \approx 1.1°$ [see (*33*) Landau fan diagram]. The main two devices we report about are devices A and B, with twist angles of $\theta = 1.09°$ and $\theta = 1.08°$, respectively. We also studied a third device C with $\theta = 1.07°$ [shown in (*33*)], which exhibits very similar behaviors. The low-energy bands in TBG are fourfold degenerate (owing to spin and valley degrees of freedom) and can support an electron density of $n_s = 4/A$, where A is the area of a moiré unit cell. This density corresponds to filling four electrons or holes per moiré unit cell. Near the first magic angle, correlated states can form at integer electron fillings of the moiré superlattice—i.e. when $n = \pm n_s/4, \pm n_s/2, \pm 3n_s/4$—where electronic interactions are believed to become comparable to the bandwidth of the nearly flat bands. In the resistivity measurements of device A [shown in Fig. 1B], we indeed find an enhancement of the resistivity ρ_{xx} at all these integer fillings. A superconducting dome is recognizable upon hole-doping of the $-n_s/2$ insulating state, at temperatures below 2.5 K. Figure 1C shows the $\rho_{xx}(T)$ curves of device A and device B at their optimal doping levels (highest T_c), where T is the sample temperature. Both devices exhibit a T_c in the range of 2.5 to 3 K (at 50% normal resistance), which is among the highest in our MATBG devices (Fig. 1E). Figure 1D shows the evolution of the V_{xx}-I_{bias} curves with temperature. From the log-log plot shown in the inset, we can extract the Berezinskii-Kosterlitz-Thouless (BKT) transition temperature to be $T_{BKT} \approx 2.2$ K. Devices A and B have some of the highest transition temperatures among all reported magic-angle TBG devices so far (table S1 and fig. S4), as evident from the T_c statistics shown in Fig. 1E, as well as devices reported in the literature (*26*, *30*, *34*).

Anisotropic behavior in the normal phase

Figure 2, A and B, show the resistivity versus gate-induced density, n, and temperature, T, maps of devices A and B, respectively, in the vicinity of $-n_s/2$. In both devices, the $-n_s/2$ region of the phase diagram has a rather complicated structure. There are two resistive features in the normal state: one "wedge"-like feature above the superconducting dome (near -1.5×10^{12} cm^{-2} for device A and -1.4×10^{12} cm^{-2} for device B) that bends at increased temperatures, and one resistive feature on the right-hand side of the dome (near -1.3×10^{12} cm^{-2} for both devices). Whereas the latter feature corresponds to the $-n_s/2$ state, similar to the correlated states previously reported in magic-angle TBG (*25*, *26*, *30*, *34*), the wedge-like feature creates a noticeable "kink" (i.e., decrease in T_c) where it approaches the superconducting dome. To further probe the resistive wedge-like feature, we apply a small perpendicular magnetic field to fully suppress superconductivity (Fig. 2, C and D). Line cuts of the resistivity versus temperature at the densities corresponding to the "kinks" of T_c are compared in Fig. 2, E and F for the two devices. When superconductivity is suppressed, the resistive wedge-like feature turns insulating upon approaching zero temperature. A small magnetic field thus results in a superconductor-to-insulator transition at this density. In Fig. 2G, we show the gradual suppression of T_c by the perpendicular magnetic field from zero to 150 mT in device A. Above about 90 mT, the superconducting dome splits at $n \approx -1.54 \times$

[1]Department of Physics, Massachusetts Institute of Technology, Cambridge, MA 02139, USA. [2]Research Center for Functional Materials, National Institute for Materials Science, Namiki 1-1, Tsukuba, Ibaraki 305-0044, Japan. [3]International Center for Materials Nanoarchitectonics, National Institute for Materials Science, Namiki 1-1, Tsukuba, Ibaraki 305-0044, Japan. [4]School of Physics and Astronomy, University of Minnesota, Minneapolis, MN 55455, USA.
*Corresponding author. Email: caoyuan@mit.edu (Y.C.); pjarillo@mit.edu (P.J.-H.)

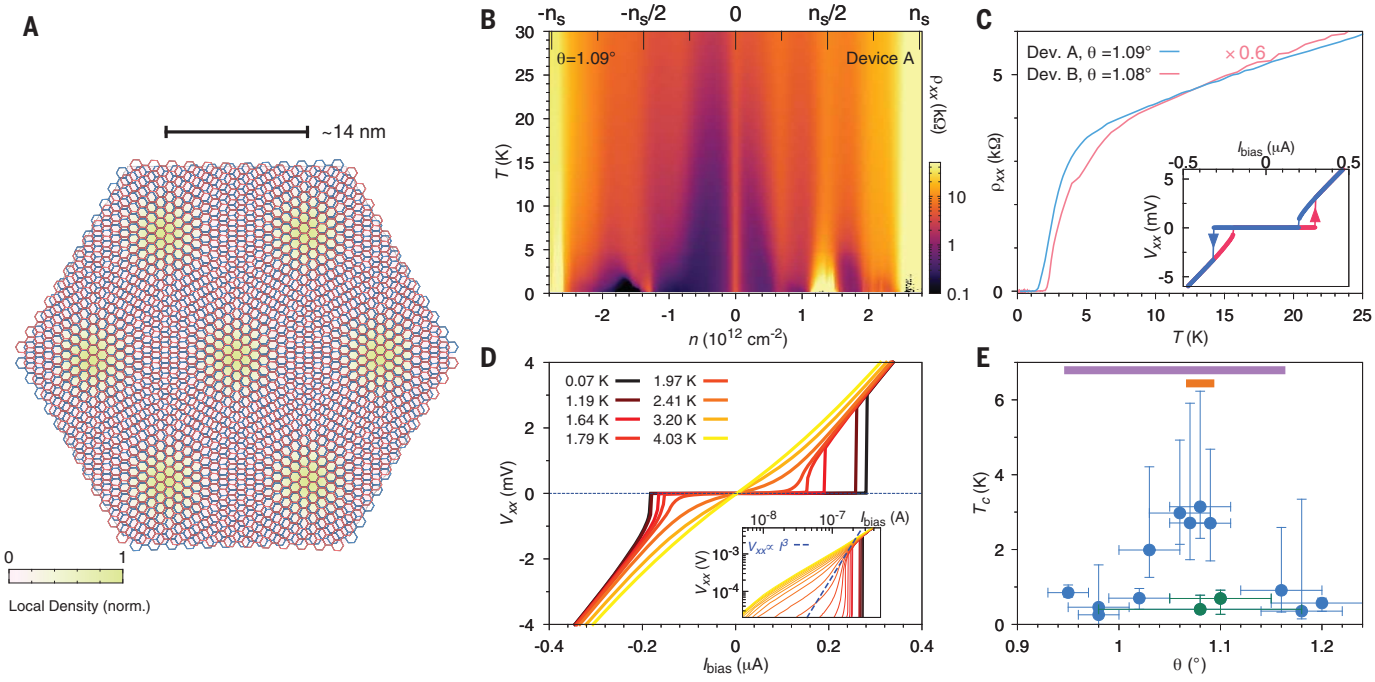

Fig. 1. Characterization and statistics of magic-angle twisted bilayer graphene (TBG) devices. (**A**) Illustration of the moiré pattern in magic-angle TBG. The color scale shows the normalized local density in the flat bands when the twist angle is close to the magic angle. The twist angle of the displayed pattern is exaggerated for clarity. (**B**) Resistivity of device A (twist angle $\theta = 1.09°$) versus gate-induced carrier density and temperature, showing correlated features at all integer electron fillings of the superlattice. Superconductivity is found at hole doping of the $-n_s/2$ insulator with critical temperature ~2.5 K. (**C**) Resistivity versus temperature for devices A and B, with twist angles $\theta = 1.09°$ and $\theta = 1.08°$, respectively, at their optimal doping concentrations. Inset: Forward and backward sweeps of the V_{xx}-I_{bias} curves in device B, which exhibit a considerable hysteresis. (**D**) Temperature dependence of the V_{xx}-I_{bias} curves measured in device B. Inset: Log-log plot of the $I > 0$ part of the data. The Berezinskii-Kosterlitz-Thouless transition temperature $T_{BKT} \approx 2.2$ K is identified where the slope of the curve crosses $d(\log V_{xx})/d(\log I_{bias}) = 3$ (equivalent to $V_{xx} \propto I_{bias}^3$). (**E**) Statistics of optimal doping T_c in 14 of the magic-angle TBG devices that we have measured. We find that T_c peaks around 1.1°, the theoretically predicted first magic-angle in TBG. The green data points are from devices exhibiting substantial disorder, hence the large error bars in the twist angle determination. This disorder may be responsible for the relatively low T_c. The orange and purple bars denote the range of twist angles where we have observed anisotropic normal-state and nematic superconductivity, respectively. The latter has been seen in all the devices where it was investigated (see table S1), spanning from $\theta = 0.95°$ to $\theta = 1.16°$. The error bar in temperature represents T_c determined from 10 and 90% of normal resistance, respectively (*33*).

10^{12} cm^{-2} into two domes. This density approximately coincides with the density at which the wedge-like feature extrapolates to zero temperature. The separated domes are centered at around -1.52×10^{12} cm^{-2} and -1.67×10^{12} cm^{-2}, respectively. The position of the splitting point corresponds to 15 ± 5% hole doping with respect to the correlated insulator state. These findings are reminiscent of the behavior in certain underdoped cuprates near 1/8 doping (*3*, *15*, *16*, *35*).

To gain more insight into the possible origin of the resistive wedge-like feature, we measure the transverse voltage across the sample at zero magnetic field, which gives the transverse resistance $R_{xy} = V_y/I_x$ (*36*, *37*). In an anisotropic conductor in two dimensions, the 2-by-2 resistivity tensor has two diagonal components $\rho = \mathrm{diag}\{\rho_1, \rho_2\}$. If the major axis of the anisotropy (usually one of the crystal axis) is not aligned with the reference frame of the tensor, the off-diagonal terms of the resistivity tensor are proportional to $(\rho_1 - \rho_2)\sin(2\theta)$, where θ is the angle between the anisotropy axis and the reference x axis [see (*33*) for derivation]. As a result, when an electrical current I_x flows in the x direction, a transverse voltage V_y appears across the edges perpendicular to the y axis, giving a nonvanishing $R_{xy} = V_y/I_x \propto (\rho_1 - \rho_2)\sin(2\theta)$, as long as $\sin(2\theta) \neq 0$ and $\rho_1 \neq \rho_2$. The first condition is assumed to be true in our experiment because the lattice orientation is random with respect to the sample edge. Consequently, a nonvanishing transverse resistance in our experiment implies anisotropic resistivity, $\rho_1 \neq \rho_2$, and therefore the breaking of the sixfold rotational symmetry of TBG. This transverse voltage is fundamentally different from the Hall effect considering that time-reversal symmetry is not broken. To quantitatively analyze the transverse voltage, it is necessary to remove any residual longitudinal component that might appear in the transverse voltage owing to imperfect alignment of the four-probe voltage contacts and/or sample inhomogeneity (*33*, *36*). Figure 3A shows the raw R_{xx} and R_{xy} measured for device A near the wedge-like feature, as shown in Fig. 2A. At high temperatures (40 K), where the anisotropies associated with electron correlation effects are presumably overwhelmed by thermal fluctuations, both R_{xx} and R_{xy} are linear in T and proportional to each other: $R_{xy} \approx -0.05R_{xx}$ (*36*). To correct for this background signal that is likely a result of the imperfect voltage probe alignment, we subtract this R_{xx} component from R_{xy} so that at the highest temperature of 40 K, the net signal is zero. This corrected transverse voltage $R_{xy}^{cr} = R_{xy} - \alpha(n)R_{xx}$, where $\alpha(n)$ is a density-dependent numerical factor typically within ±0.1, constitutes an accurate measure of the resistivity anisotropy (purple curve in Fig. 3A). Whereas no signal is present at higher temperatures, below 6 K there is a pronounced negative peak in R_{xy}^{cr}, which indicates the onset of anisotropy at this temperature.

The gate and temperature dependence of the anisotropy, shown in Fig. 3, B and C, for zero magnetic field and $B_\perp = 0.5$ T (*33*), clearly reveals a prominent anisotropy wedge as well. The transverse voltage measured at $B_\perp = 0.5$ T is symmetrized with data measured at $B_\perp =$

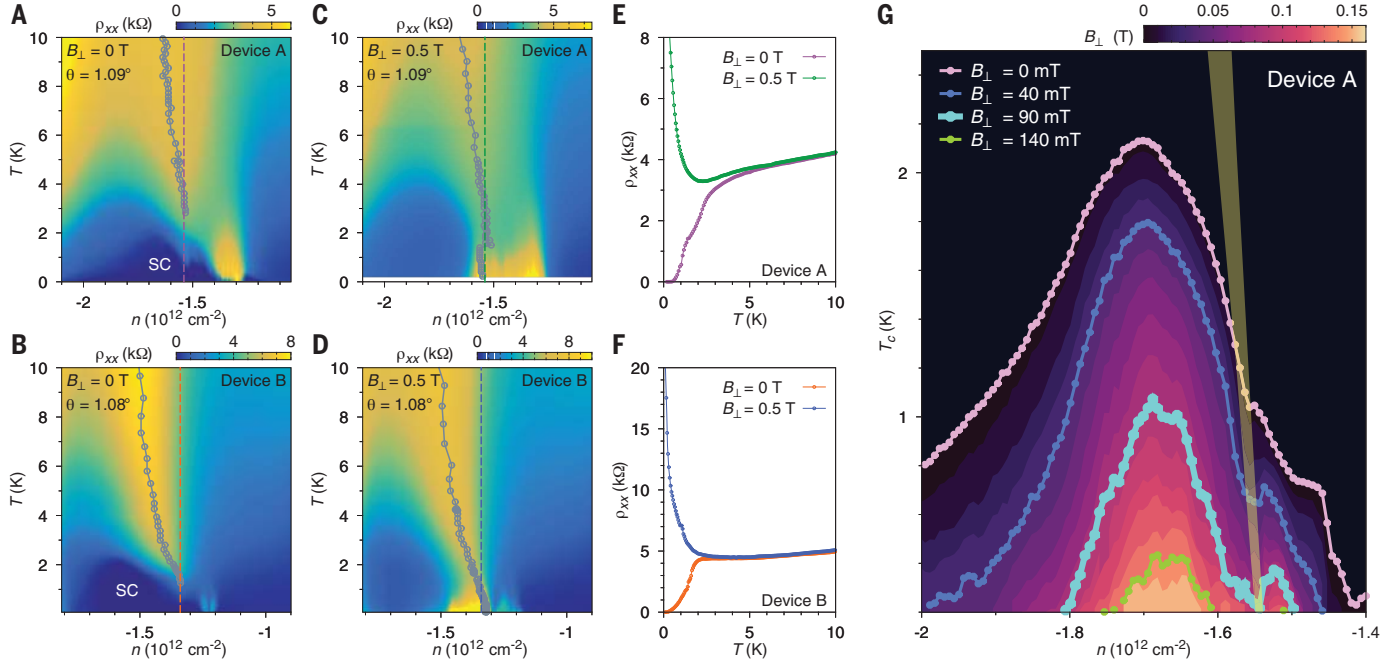

Fig. 2. Competing phases near the superconducting domes of magic-angle TBG. (**A** and **B**) Resistivity versus gate-induced carrier density and temperature for device A and device B, respectively. (**C** and **D**) Same measurement but in a perpendicular magnetic field of 0.5 T. (**E** and **F**) Line cuts of resistivity versus temperature for devices A and B at 0 and 0.5 T at the densities indicated by the dashed lines in (A) to (D), showing a superconductor-to-insulator transition induced by the magnetic field. In both devices, we find a wedge-like feature above the superconducting dome in addition to the $-n_s/2$ correlated state. The gray circles in (A) to (D) indicate the resistivity maxima associated with the wedge-like feature at different temperatures. (**G**) Evolution of T_c of device A in a perpendicular magnetic field up to 0.15 T. Each contour line is T_c (10% normal resistance) versus carrier density at the magnetic field indicated by the color shading. Contour lines for four values of the magnetic field are highlighted in contrasting colors. The yellow band represents the approximate position of the wedge-like feature. At $B_\perp$ = 0.09 T (light blue curve), the T_c kink touches zero at the same density where the wedge-like feature extrapolates to zero temperature. Above this field, the superconducting dome splits into two domes roughly centered at -1.52×10^{12} cm^{-2} and -1.67×10^{12} cm^{-2}, respectively.

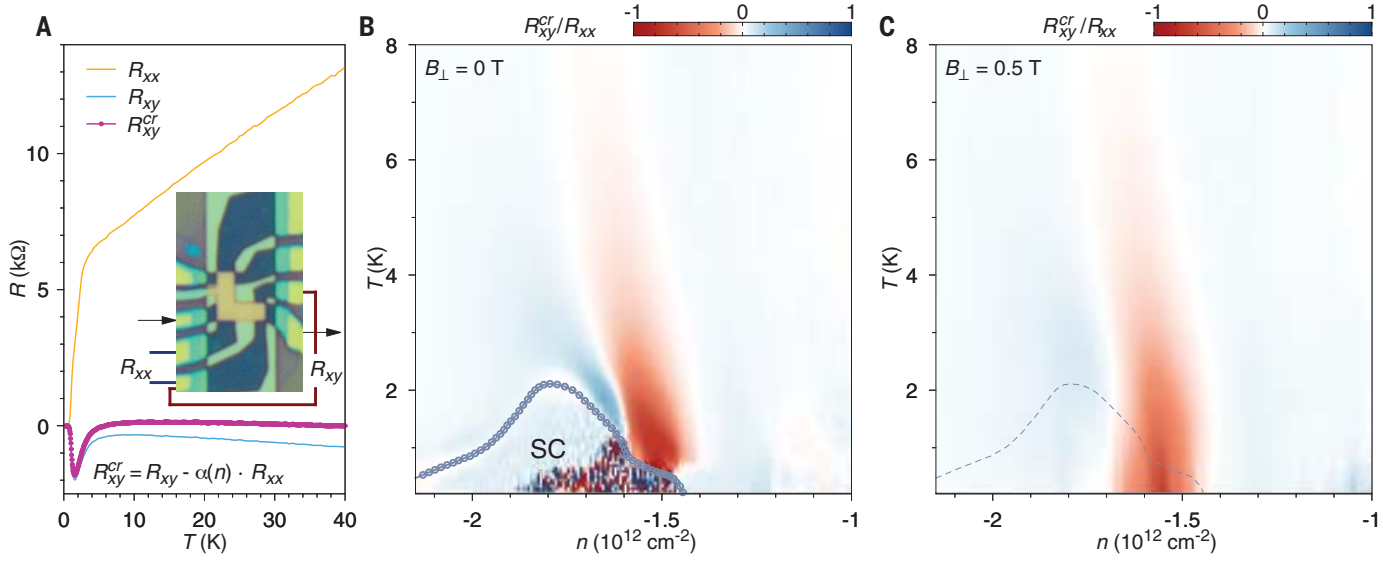

Fig. 3. Normal-state anisotropy in magic-angle TBG device A. (**A**) Inset shows the device configuration that we used to measure the transverse resistance, with black arrows indicating current source and drain. R_{xx}, R_{xy} label the leads on which longitudinal and transverse resistances are measured, respectively. The purple trace, R_{xy}^{cr}, is the transverse resistance corrected for leads misalignment (*33*). $n = -1.53 \times 10^{12}$ cm^{-2} in this measurement. (**B** and **C**) Anisotropy ratio versus carrier density and temperature at zero magnetic field and $B_\perp$ = 0.5 T, respectively (*33*). The circles in (B) and the dashed line in (C) outline the approximate shape of the superconducting dome (at zero field). We find the strongest anisotropy near the kink in T_c at $n = -1.54 \times 10^{12}$ cm^{-2}, coinciding with the resistive wedge-like feature we identified in Fig. 2, A and G.

−0.5 T to remove the contribution from the Hall voltage. Here we plot the normalized quantity R_{xy}^{cr}/R_{xx}, which is approximately proportional to the anisotropy ratio $(\rho_1 - \rho_2)/(\rho_1 + \rho_2)$ (*33*). We also mark out the superconducting dome in Fig. 3, B and C. Immediately above the superconducting dome on the "underdoped" side (lower $|n|$), we find a strong transverse voltage signal with a sign change at around -1.59×10^{12} cm^{-2} (see fig. S2 for the entire range of density). The position of the anisotropy wedge matches well that of the resistive wedge-like feature that we observed in Fig. 2A. The sign change indicates that the anisotropy changes from $\rho_1 > \rho_2$ to $\rho_1 < \rho_2$ (or vice versa). In $B_\perp = 0.5$ T (Fig. 3C), the anisotropy wedge with negative values of R_{xy}^{cr} persists to zero temperature, consistent with the behavior of the resistive wedge-like feature in Fig. 2B. However, we notice that the anisotropy with positive R_{xy}^{cr} near -1.65×10^{12} cm^{-2} disappears as superconductivity is suppressed by the magnetic field, which might be explained by the vestigial order from the nematic superconductivity that will be discussed in the next section.

Nematic superconducting state

A natural question to ask is whether the superconducting phase exhibits any anisotropic properties as well. To investigate this, we measure the angle-dependent in-plane magnetic field response of the superconducting phase. In magic-angle TBG, the superconductivity is suppressed by an in-plane magnetic field of the same order of magnitude as the Pauli paramagnetic limit (*26*). Using a vector magnet in a dilution refrigerator, we apply a magnetic field $B_{||}$ up to 1 T in an arbitrary direction within the sample plane (Fig. 4A). We compensate for possible sample tilt by applying a small out-of-plane magnetic field, so that the magnetic field is parallel to the sample to within $|B_\perp| < 2$ mT at $|B_{||}| = 1$ T, which is much less than the perpendicular critical magnetic field of our devices [see (*33*) and fig. S3 for detailed calibration procedure, and see fig. S5 for the perpendicular critical magnetic field of devices A and B]. Figure 4B shows an example of the resistivity versus in-plane magnetic field magnitude $|B_{||}|$ and angle θ_B (with respect to the length of the Hall bar; Fig. 4A). A twofold anisotropic suppression of the superconductivity (emergence of a finite dissipation) can be clearly seen. We have checked that the direction of the current flow is not correlated with the anisotropy direction, and therefore the anisotropic Lorentz force contribution can be excluded (fig. S6). The anisotropy is not aligned with the length or width of the Hall bar either (fig. S6).

The twofold anisotropy of the in-plane magnetotransport response points toward nematicity that is intrinsic to the superconducting

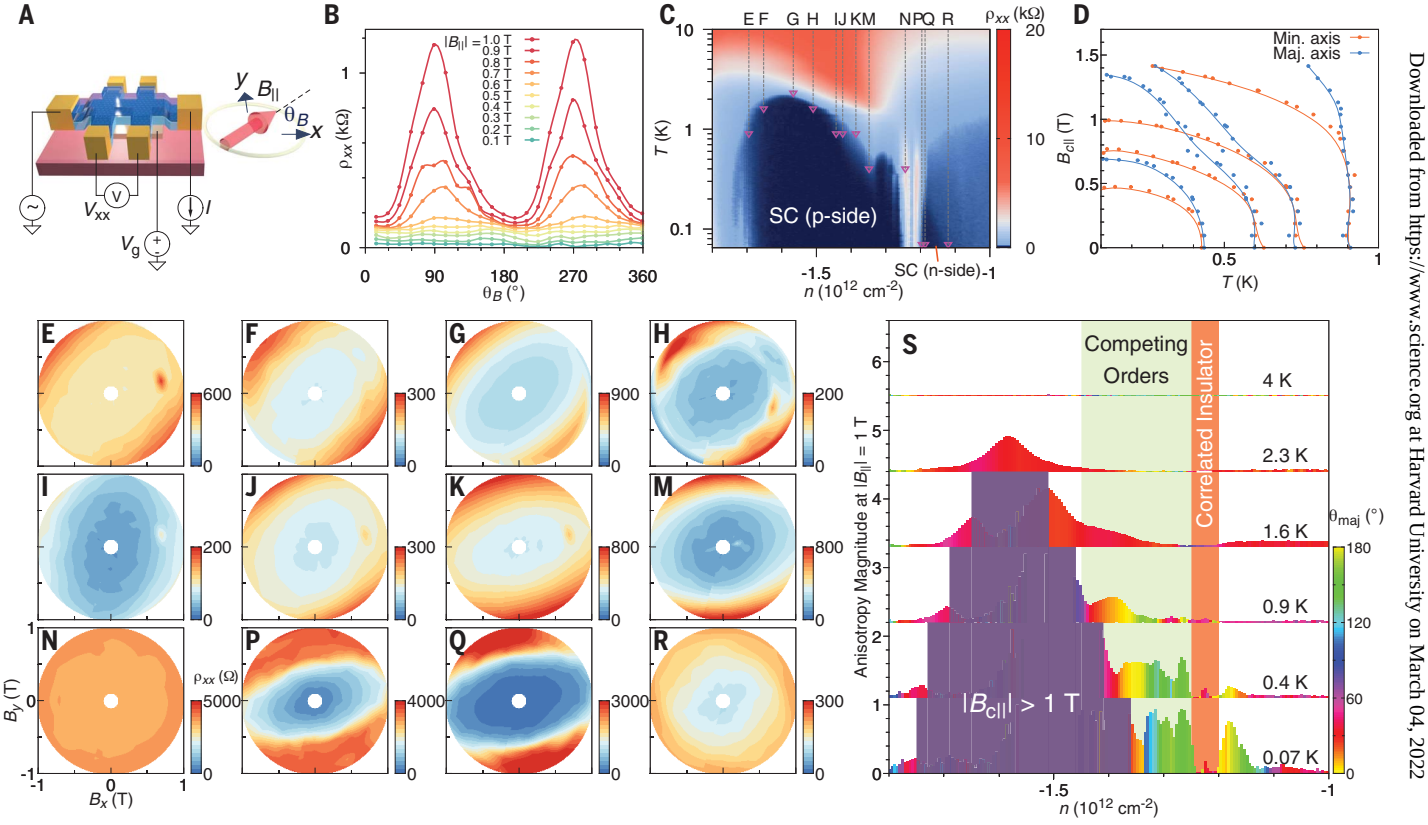

Fig. 4. Evidence for nematic superconductivity in magic-angle TBG. (**A**) Schematic of the Hall bar device. The in-plane field angle θ_B is defined with respect to the source-drain direction (x axis). (**B**) Resistivity as a function of θ_B for different magnitudes of the in-plane magnetic field, showing a clear two-fold anisotropy. Measurement is taken at $n = -1.18 \times 10^{12}$ cm^{-2} and $T = 70$ mK in device B. (**C**) Detailed view of the superconducting domes in device B, showing a large and a small superconducting dome on the p-side and n-side of the insulating state. (**D**) Critical in-plane magnetic field $B_{c||}$ versus temperature along the major and minor axis of the twofold anisotropy, measured in device A at carrier densities of -1.44×10^{12}, -1.42×10^{12}, -1.40×10^{12}, and -1.23×10^{12} cm^{-2} (from right to left). (**E** to **R**) Polar maps of the anisotropic response of the resistivity across the superconducting domes in device B. The carrier densities and temperatures at which (E) to (R) are measured correlate with the labels in (C). (**S**) For device B, we extracted the magnitude (represented by height) and the polar angle of the major axis θ_{maj} [represented by the color; see (*33*) for details] of the nematicity at different densities and temperatures, with $|B_{||}| =$ 1 T. The data for different temperatures are shifted vertically for clarity. Inside the region shaded in purple, the critical in-plane magnetic field is larger than 1 T and cannot be measured in our setup. In the density range of -1.45×10^{12} to -1.2×10^{12} cm^{-2}, the anisotropy polar angle θ_{maj} rotates rapidly with the carrier density, possibly owing to the competition with the wedge-like feature that we identified in Figs. 2 and 3.

phase, as it breaks the sixfold rotational symmetry of the moiré superlattice. We have systematically studied this nematic behavior across the entire superconducting dome of device B. In Fig. 4, E to R, we show polar maps of the magnetoresistivity at different carrier densities and temperatures in the hole-doping and electron-doping superconducting domes as labeled in Fig. 4C. At all densities except those in Fig. 4, N and R, we find elliptic contours that have major/minor axis ratios up to ~3. We chose to always measure near T_c, because deep inside the superconducting dome, the in-plane critical field is usually larger than 1 T and cannot be measured in our setup. However, we have confirmed the nematicity in the $T \ll T_c$ region by simultaneously applying a small perpendicular field to partially suppress the superconducting state (fig. S7). At the densities corresponding to Fig. 4, N and R, which are outside the superconducting regions, the anisotropy is essentially nonexistent. In general, the twofold anisotropy occurs inside the broad transition from superconducting to normal state as a function of $B_{||}$, suggesting that it is a property intrinsic to the superconducting fluctuations (*38*); the normal state does not show any anisotropy in the in-plane magnetoresistance (fig. S9). In device A, we have observed a similar twofold anisotropic in-plane critical field (Fig. 4D). The critical magnetic field $B_{c||}$ along the major axis extrapolated to zero temperature exceeds that along the minor axis by 40 to 80% in this device.

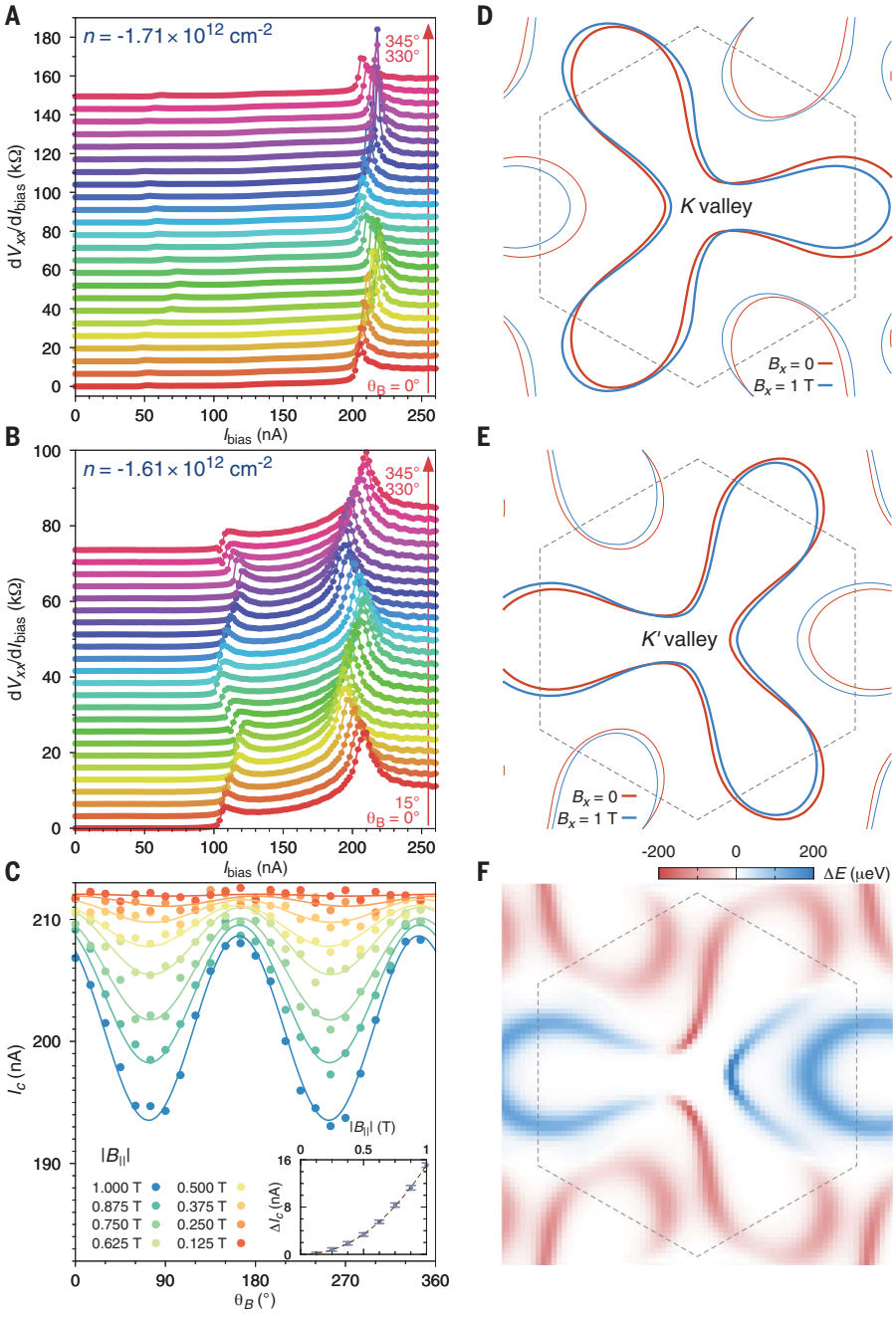

Fig. 5. Anisotropic response of the superconducting critical current. (**A** and **B**) Differential resistance dV_{xx}/dI_{bias} versus bias current I_{bias} as a function of the orientation of the in-plane magnetic field at two carrier densities. The orientation is indicated by the color, differing by 15° between adjacent curves, which are vertically shifted for clarity. (**C**) Modulation of the larger critical current in (B) by in-plane magnetic fields with different orientations and magnitudes. A sinusoidal function is used to fit the data (see main text). Inset: The modulation amplitude (peak-peak) as a function of the field magnitude, which can be fit by a power law $\Delta I_c \propto |B_{||}|^{\alpha}$ with $\alpha \approx 2.1$. (**D** and **E**) Calculated Fermi contour of θ = 1.09° TBG at $B_x = 0$ and $B_x = 1$ T around *K* and *K*′ valleys, respectively (*33*). (**F**) Energy splitting between states at opposite momentum and opposite valleys along the Fermi surface $\Delta E(\boldsymbol{k}) = E_{K'}(\boldsymbol{k}) - E_K(-\boldsymbol{k})$ at $B_x = 1$ T. For comparison, the Zeeman splitting $g\mu_B B$ at $B = 1$ T for $g = 2$ is 115 μeV. The gray hexagons in (D) to (F) denote the moiré Brillouin zone.

Figure 4S shows the evolution of the magnitude and of the director of the nematic component of the superconducting state in device B as a function of carrier density and temperature. Our data show that the nematic director, as measured by the angle of rotation of the ellipse's major axis, does not appear to be exactly locked to any particular spatial axis, but instead evolves continuously with carrier density and temperature. In particular, in the superconducting dome on the hole-doping side of $-n_s/2$, the direction of the major axis varies slowly within +20 to +50° in the density range of -1.70×10^{12} to -1.45×10^{12} cm^{-2} (corresponding to the ellipses from Fig. 4, E to H), whereas in the range of -1.45×10^{12} to -1.25×10^{12} cm^{-2} (from Fig. 4, I to M), the major axis rotates quickly with the carrier density. From Fig. 4, I to M, the major axis rotates by ~90°. The latter range of density again coincides with the resistive wedge-like feature for device B, as shown from Fig. 2, B and D. The smaller superconducting dome on the electron-doping side near -1.20×10^{12} cm^{-2} exhibits appreciable nematicity as well (Fig. 4, P and Q), with a director pointing from 150° to 190° (10°). As we explain below, that the nematic director changes direction as a function of doping and temperature makes it unlikely that the superconducting anisotropy is simply a response to strain present in the sample. On the contrary, this observation is consistent with spontaneous rotational symmetry-breaking characteristic of an intrinsic nematic superconductor.

Anisotropic response of the superconducting gap

The observation of nematicity puts certain constraints on possible pairing symmetries

of the superconducting order parameter (*14*, *39*, *40*). One can obtain information about the superconducting gap by measuring the critical current I_c. Here, by measuring I_c of device B in the presence of in-plane magnetic fields, we demonstrate that the nematicity not only is manifested in the resistivity measurements but also creates an anisotropic modulation of the superconducting gap. Figure 5, A and B, show the waterfall plots of differential resistance dV_{xx}/dI_{bias} versus dc bias current I_{bias} at two carrier densities, in an in-plane magnetic field $|B_{||}| = 1$ T along different directions indicated by the colors. At the carrier density in Fig. 5B, the plot shows two critical currents at 110 and 210 nA, respectively, which might be a consequence of domains in the device with different twist angles or nematic directors. At both carrier densities, the critical current shows notable twofold modulation by the in-plane magnetic field direction θ_B. The θ_B dependence can be fit by a sinusoidal function $\cos2(\theta_B - \theta_{B0})$ (Fig. 5C), where θ_{B0} is the direction of the major axis. The modulation amplitude as a function of the in-plane field magnitude is shown in the inset of Fig. 5C and follows an approximately quadratic power-law dependence.

An anisotropic response in the critical current may originate from (i) an anisotropic angular dependence of the superconducting gap Δ and/or (ii) anisotropic properties of the underlying normal-state resistance (R_n). Although we have shown that the normal state exhibits considerable resistivity anisotropy at densities near the wedge-like feature in Fig. 3, we argue here that the anisotropic response of the critical current is not a result of the anisotropy of R_n. First, Fig. 5A is measured at a density for which there is essentially no resistivity anisotropy in the normal state ($R_{xy}^{cr}/R_{xx} = -0.007$ at the lowest T in Fig. 3C), whereas Fig. 5B is measured at a density with considerable anisotropy in the normal state ($R_{xy}^{cr}/R_{xx} = -0.325$ at the lowest T in Fig. 3C). However, the modulation of the critical current at these two densities shows similar magnitudes. Second, an anisotropy in the resistivity tensor may not necessarily imply a large anisotropic response of the resistivity versus in-plane magnetic field. Indeed, inside the wedge-like feature in the normal state in device A, we could not measure any substantial anisotropic response to the in-plane field (fig. S9). Thus, these results suggest that the anisotropic response of the critical current might not be directly related to the resistivity anisotropy of the normal state and hence may originate from an anisotropic superconducting gap.

To discuss the mechanism by which the in-plane field couples to the superconducting gap, we note that if the former couples solely to the spin degree of freedom (and thus the gap is only suppressed by the Zeeman coupling), spin-orbit interaction must be introduced to explain the dependence of I_c on the direction of $B_{||}$. However, the intrinsic spin-orbit coupling in graphene-based systems is known to be very weak. We might consider the following mechanism to reconcile these findings. As illustrated in Fig. 1A, the unit cell of magic-angle TBG has a length scale of $a \sim 14$ nm. Despite the separation between the graphene sheets in TBG being merely $\delta \sim 0.3$ nm, an in-plane magnetic field that threads through the space between them induces a small but non-negligible magnetic flux in the cross-section of the unit cell with an area $S \sim a\delta$, which modifies the Fermi contours. To demonstrate this effect, we numerically calculated the Fermi contours at $-n_s/2$ for $B_{||} = 0$ and $B_{||} = 1$ T along the x direction using the Bistritzer-MacDonald continuum model (*28*). Figure 5, D and E, show the original and modified Fermi contours for the K and K' valleys, respectively; a noticeable shift is induced by the in-plane magnetic field. The K/K' valley degeneracy is lifted by the momentum shift between the two layers introduced by the in-plane field, which is proportional to $e\delta B_{||}$, a substantial shift given the small size of the Brillouin zone. If one assumes that only electrons with opposite momentum and valley are allowed to form Cooper pairs in the superconducting phase, the two states from opposite valleys would be at slightly different energies when an in-plane field is applied, which serves to suppress the superconductivity in a manner similar to that of the paramagnetic (Zeeman) effect in the case of spins. To more intuitively demonstrate this, Fig. 5F shows the depairing energy along the Fermi contour $\Delta E(\boldsymbol{k}) = E_K(\boldsymbol{k}) - E_K(-\boldsymbol{k})$. It is strongly direction dependent and has an order of magnitude similar to that of the Zeeman energy at $B_{||} = 1$ T ($g\mu_B B_{||} \approx 115$ μeV, where $g = 2$ and μ_B is the Bohr magneton). The depairing energy exhibits a six-fold variation with respect to the direction of the in-plane magnetic field, whereas the nematic component of the superconducting order can further spontaneously break this symmetry down to the observed twofold symmetry (*38*, *39*, *41*). A small strain can further assist to pin down the nematic domain along a given direction.

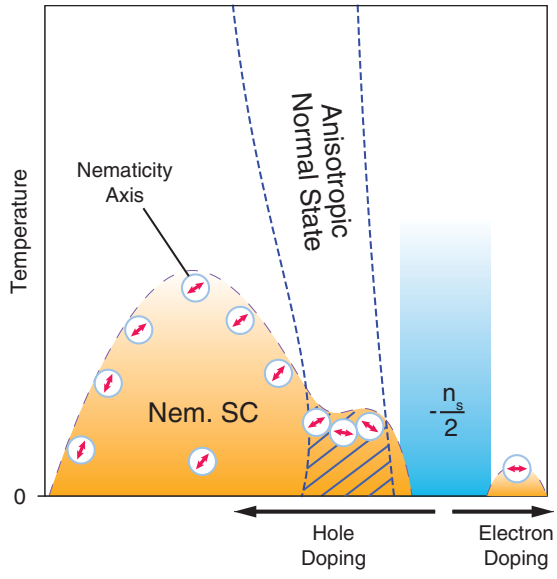

Fig. 6. Summary of various competing phases. On the underdoped side of the superconducting dome, we find a normal-state anisotropic phase that, at low temperatures, competes with superconductivity, creating a depression in the T_c curve. In the superconducting state, we find nematicity, manifested in its response to in-plane magnetic fields. By comparing the extracted nematicity temperature T_{nem} to T_c, we find that the entire superconducting dome exhibits nematicity, which suggests that the nematicity is intrinsic to the superconductivity and points toward a possible unconventional pairing symmetry. The dashed area denotes the competing region between the two states, where a reduction in T_c, as well as a strong rotation of the nematicity axis, is seen.

Discussion

Our measurements reveal two distinct anisotropic states in the phase diagram of magic-angle TBG: a normal-state wedge-like feature above the superconducting dome and a nematic superconducting state. The wedge-like feature is associated with a zero-temperature insulating phase that shows appreciable resistivity anisotropy, indicative of broken sixfold lattice rotational symmetry. Thus, this normal-state phase might be either an electronic nematic state or an electronic smectic state—i.e., a charge or spin-density wave that, in addition to rotational symmetry, also breaks translational lattice symmetry. In either case, the rotational symmetry breaking can be described by a two-component three-state Potts nematic order parameter (*41*, *42*). Electronic correlations might be important for the formation of such a state. Twisted bilayer graphene is well-known to exhibit van Hove singularities (vHs), which in general do not occur exactly at half-filling (*43*, *44*). Near the vHs, it has been theoretically shown that the considerable nesting between the K- and K'-valley Fermi contours might induce density wave ordering (*40*). Notably, recent scanning tunneling experiments have identified prominent rotational-symmetry–broken features in the normal-state local density of states (*45*–*47*). Alternatively, strong-coupling models can also yield nematic and density-wave states (*48*, *49*). For the superconducting phase, it remains to be seen whether its

nematic character, as revealed by the measured in-plane anisotropy of the critical field, can be reconciled with *s*-wave pairing. This behavior could be explained in terms of a two-component *p*-wave/*d*-wave gap, indicative of an unconventional pairing mechanism (*50*).

A crucial question is whether the anisotropies observed here have intrinsic or extrinsic origins. The observation that we do not observe multiple nematic domains within the same device implies that some degree of residual strain is present. The issue is whether this strain is the sole cause of the anisotropy (extrinsic origin) or is mainly pinning one of the three underlying nematic domains (intrinsic origin). To address this, we note that such a residual strain should be a property of the device and thus should be present at all temperatures and doping. By contrast, as shown in Fig. 3, the onset of the normal-state anisotropy is restricted to a narrow doping range and to temperatures below 10 K. Furthermore, the resistance anisotropy is on the order of one in the wedge-like feature (see Fig. 3B). Such a large effect would be difficult to attribute to a reasonably sized residual strain.

These quantitative arguments rely on the amplitude of the anisotropy, but a more direct argument against an extrinsic origin can be made from the direction of the anisotropy. Our measurements in the superconducting state clearly show a rotation of the nematic director (Fig. 4, E to S). In the three-state Potts model, the three states correspond to the three nearest-neighbor directions in the moiré superlattice (*41*). Here, strain acts as a conjugate field to the nematic order parameter, similarly to how a magnetic field acts on a ferromagnet. If the strain is "parallel" to one of the three anisotropy directions, the corresponding nematic director is favored over the other two. As a result, the nematic director is fixed at all temperatures. If the strain is "antiparallel" to a direction, the other two directions become favored. Consequently, as the temperature is lowered toward the nematic state, the nematic director continuously rotates from the disfavored direction to one of the two favored directions (*41*). Notably, this can only happen if nematic order is spontaneous; i.e., if it is an intrinsic instability of the system (*33*). Therefore, the continuous rotation of the nematic director in our observation indicates that the anisotropy of the superconducting state is more likely to be intrinsic, as an extrinsic origin would result in a fixed orientation.

Another possible source of anisotropy is twist angle variations across the device, which could create an inhomogeneous distribution of strain (*51*). Although further studies are needed, we note that such an inhomogeneous strain would act as a random field to the Potts-nematic order parameter, which might affect the nematic properties in 2D (*52*). However, that we do not see different nematic domains across our device suggests that the global residual strain is probably dominating over the local strain caused by twist angle fluctuations.

The various phases discussed throughout this article are summarized in Fig. 6 [see (*33*) and fig. S8 for the extracted nematicity temperature T_{nem}]. An anisotropic response to an in-plane magnetic field is seen only in the superconducting state, but not in the wedge-like feature, suggesting that the origins of nematicity in the normal and superconducting states are likely different. This is also consistent with the observation that these two orders compete, as evident from the suppression of T_c when the wedge-like feature meets the superconducting dome. However, because both phases break the same sixfold lattice rotational symmetry, the order parameters of these two phases can interact beyond mere competition, which may be responsible for the rapid change of the ellipse direction in the part of the phase diagram below the wedge (*33*). Moreover, normal-state nematic fluctuations may play an important role in favoring a superconducting ground state that is also nematic. Although the onsets of nematicity and of superconductivity seem very close in our experiment (*33*), it is possible that the nematic order in magic-angle TBG persists even above T_c, a phenomenon known as vestigial nematic order (*12*, *14*, *42*). In Fig. 3B, there is a region just above the superconducting dome with positive transverse voltage signal at $n \approx -1.65 \times 10^{12}$ cm^{-2} and $T \approx 2$ K. This signal not only has the opposite sign of the anisotropy of the wedge-like state, but it also disappears when superconductivity is suppressed (Fig. 3C). Thus, this feature might be explained by a vestigial nematic order that forms before the condensation of Cooper pairs (*12*, *14*, *42*). Scanning probe experiments are needed to confirm this nematic phase above the superconducting transition.

REFERENCES AND NOTES

1. P. W. Anderson, *Science* **177**, 393–396 (1972).
2. S. Sachdev, *Rev. Mod. Phys.* **75**, 913–932 (2003).
3. B. Keimer, S. A. Kivelson, M. R. Norman, S. Uchida, J. Zaanen, *Nature* **518**, 179–186 (2015).
4. E. Fradkin, S. A. Kivelson, M. J. Lawler, J. P. Eisenstein, A. P. Mackenzie, *Annu. Rev. Condens. Matter Phys.* **1**, 153–178 (2010).
5. R. M. Fernandes, A. V. Chubukov, J. Schmalian, *Nat. Phys.* **10**, 97–104 (2014).
6. V. Hinkov *et al*., *Science* **319**, 597–600 (2008).
7. J.-H. Chu, H.-H. Kuo, J. G. Analytis, I. R. Fisher, *Science* **337**, 710–712 (2012).
8. T.-M. Chuang *et al*., *Science* **327**, 181–184 (2010).
9. E. P. Rosenthal *et al*., *Nat. Phys.* **10**, 225–232 (2014).
10. B. E. Feldman *et al*., *Science* **354**, 316–321 (2016).
11. Y. Sato *et al*., *Nat. Phys.* **13**, 1074–1078 (2017).
12. L. Nie, G. Tarjus, S. A. Kivelson, *Proc. Natl. Acad. Sci. U.S.A.* **111**, 7980–7985 (2014).
13. E. Fradkin, S. A. Kivelson, J. M. Tranquada, *Rev. Mod. Phys.* **87**, 457–482 (2015).
14. R. M. Fernandes, P. P. Orth, J. Schmalian, *Annu. Rev. Condens. Matter Phys.* **10**, 133–154 (2019).
15. C. Proust, L. Taillefer, *Annu. Rev. Condens. Matter Phys.* **10**, 409–429 (2019).
16. J. Chang *et al*., *Nat. Phys.* **8**, 871–876 (2012).
17. S. D. Edkins *et al*., *Science* **364**, 976–980 (2019).
18. J. Li *et al*., *Nat. Commun.* **8**, 1880 (2017).
19. J. Shen *et al*., *npj Quantum Mater.* **2**, 59 (2017).
20. A. Y. Kuntsevich *et al*., *New J. Phys.* **20**, 103022 (2018).
21. K. Matano, M. Kriener, K. Segawa, Y. Ando, G. Zheng, *Nat. Phys.* **12**, 852–854 (2016).
22. T. Asaba *et al*., *Phys. Rev. X* **7**, 011009 (2017).
23. Y. Pan *et al*., *Sci. Rep.* **6**, 28632 (2016).
24. M. P. Smylie *et al*., *Sci. Rep.* **8**, 7666 (2018).
25. Y. Cao *et al*., *Nature* **556**, 80–84 (2018).
26. Y. Cao *et al*., *Nature* **556**, 43–50 (2018).
27. E. Suárez Morell, J. D. Correa, P. Vargas, M. Pacheco, Z. Barticevic, *Phys. Rev. B Condens. Matter Mater. Phys.* **82**, 121407 (2010).
28. R. Bistritzer, A. H. MacDonald, *Proc. Natl. Acad. Sci. U.S.A.* **108**, 12233–12237 (2011).
29. J. M. B. Lopes dos Santos, N. M. R. Peres, A. H. Castro Neto, *Phys. Rev. B Condens. Matter Mater. Phys.* **86**, 155449 (2012).
30. M. Yankowitz *et al*., *Science* **363**, 1059–1064 (2019).
31. Y. Cao *et al*., *Phys. Rev. Lett.* **117**, 116804 (2016).
32. K. Kim *et al*., *Nano Lett.* **16**, 1989–1995 (2016).
33. See supplementary materials.
34. X. Lu *et al*., *Nature* **574**, 653–657 (2019).
35. B. J. Ramshaw *et al*., *Science* **348**, 317–320 (2015).
36. P. Walmsley, I. R. Fisher, *Rev. Sci. Instrum.* **88**, 043901 (2017).
37. J. Wu, A. T. Bollinger, X. He, I. Božović, *Nature* **547**, 432–435 (2017).
38. J. W. F. Venderbos, V. Kozii, L. Fu, *Phys. Rev. B* **94**, 094522 (2016).
39. V. Kozii, H. Isobe, J. W. F. Venderbos, L. Fu, *Phys. Rev. B* **99**, 144507 (2019).
40. H. Isobe, N. F. Q. Yuan, L. Fu, *Phys. Rev. X* **8**, 041041 (2018).
41. R. M. Fernandes, J. W. F. Venderbos, *Sci. Adv.* **6**, eaba8834 (2020).
42. M. Hecker, J. Schmalian, *npj Quantum Mater.* **3**, 26 (2018).
43. G. Li *et al*., *Nat. Phys.* **6**, 109–113 (2010).
44. A. Luican *et al*., *Phys. Rev. Lett.* **106**, 126802 (2011).
45. A. Kerelsky *et al*., *Nature* **572**, 95–100 (2019).
46. Y. Jiang *et al*., *Nature* **573**, 91–95 (2019).
47. S.-Y. Li *et al*., *Phys. Rev. B* **96**, 155416 (2017).
48. J. Kang, O. Vafek, *Phys. Rev. Lett.* **122**, 246401 (2019).
49. J. F. Dodaro, S. A. Kivelson, Y. Schattner, X. Q. Sun, C. Wang, *Phys. Rev. B* **98**, 075154 (2018).
50. D. V. Chichinadze, L. Classen, A. V. Chubukov, *Phys. Rev. B* **102**, 125120 (2020).
51. A. Uri *et al*., *Nature* **581**, 47–52 (2020).
52. D. Blankschtein, Y. Shapir, A. Aharony, *Phys. Rev. B Condens. Matter* **29**, 1263–1267 (1984).
53. Y. Cao *et al*., Replication Data for: Nematicity and Competing Orders in Superconducting Magic-Angle Graphene, Version 1.0, Harvard Dataverse (2021).

ACKNOWLEDGMENTS

We acknowledge helpful discussions with P. A. Lee, S. Todadri. A. Vishwanath, A. Hristov, I. Fisher, J. Venderbos, and S. A. Kivelson. **Funding:** This work was supported by the STC Center for Integrated Quantum Materials (NSF grant no. DMR-1231319) for most devices' fabrication, transport measurements, and data analysis (Y.C., D.R.-L.). J.M.P. acknowledges the US Department of Energy (DOE), Office of Basic Energy Sciences (BES), Division of Materials Sciences and Engineering under Award DE-SC0001819 for additional device fabrication. D.R.-L. acknowledges partial support from Fundación Bancaria "la Caixa" (LCF/BQ/AN15/10380011) and from the US Army Research Office (grant no. W911NF-17-S-0001). P.J.-H. acknowledges support from the Gordon and Betty Moore Foundation's EPiQS Initiative through grant GBMF9643 and the National Science Foundation (DMR-1809802). The development of new nanofabrication and characterization techniques enabling this work has been supported by the US DOE Office of Science, BES, under award DE-SC0019300. K.W. and T.T. acknowledge support from the Elemental Strategy Initiative conducted by MEXT, Japan (grant no. JPMXP0112101001), JSPS KAKENHI (grant no. JP20H00354), and CREST (JPMJCR15F3), JST. This work made use of the Materials Research Science and Engineering Center Shared Experimental Facilities supported by

the National Science Foundation (DMR-0819762) and of Harvard's Center for Nanoscale Systems, supported by the NSF (ECS-0335765). R.M.F. (phenomenological modeling) acknowledges support by the U.S. Department of Energy, Office of Science, Basic Energy Sciences, Materials Sciences and Engineering Division, under Award no. DE-SC0020045. N.F.Q.Y. and L.F. (in-plane field modeling) were supported by the US DOE, Office of Science, Office of Basic Energy Sciences (BES), Division of Materials Sciences and Engineering under Award DE-SC0018945; **Author contributions:** Y.C., D.R.-L., and J.M.P. fabricated samples and performed transport measurements. Y.C., D.R.-L., and P.J.-H. performed data analysis and discussed the results. P.J.-H. supervised the project. N.F.Q.Y., L.F., and R.M.F. provided theoretical support. K.W. and T.T. provided h-BN samples. Y.C., D.R.-L., and P.J.-H. co-wrote the manuscript with input from all coauthors. **Competing interests:** The authors declare no competing financial interest. **Data and materials availability:** The data from this study are available at the Harvard Dataverse (*53*).

SUPPLEMENTARY MATERIALS

science.sciencemag.org/content/372/6539/264/suppl/DC1
Materials and Methods
Figs. S1 to S12
Table S1
References (*54*–*61*)

16 April 2020; accepted 12 March 2021
10.1126/science.abc2836

Nematicity and competing orders in superconducting magic-angle graphene

Yuan CaoDaniel Rodan-LegrainJeong Min ParkNoah F. Q. YuanKenji WatanabeTakashi TaniguchiRafael M. FernandesLiang FuPablo Jarillo-Herrero

Science, 372 (6539), • DOI: 10.1126/science.abc2836

Twisted and nematic

Electrons in quantum materials can break rotational symmetry even when the underlying crystal lattice does not. This phenomenon, called nematicity, has been observed in many unconventional superconductors. Cao *et al.* found that magic-angle twisted bilayer graphene, in which superconductivity was recently discovered, also exhibits nematicity. The breaking of rotational symmetry was observed through transport measurements, which exhibited characteristic anisotropy.

Science, this issue p. 264